




Numerical investigation of forces and acceleration for air-sea unmanned aerial vehicle in transition

Emmanuel C. Chukwuemeka¹ · Forrest Ames¹ · Razaq A. Kazeem² · Moses O. Petrinrin² · Omolayo M. Ikumapayi^{3,4}  · Esther T. Akinlabi⁵

Received: 3 December 2022 / Accepted: 17 April 2023

© The Author(s), under exclusive licence to Springer-Verlag France SAS, part of Springer Nature 2023

Abstract

The air-sea UAV is made to be able to fly, change from land to water, and navigate through submerged water. However, as it moves from the air to the water, it experiences a significant impact force. The UAV's structure and components run the risk of being harmed by this strong impact force. The accelerations and forces involved in the transition process must therefore be understood through quantitative research. The method was created using computational fluid dynamics (CFD), which can manage the process of water entry. The simulation and calculations were carried out using the Fluent software suite from ANSYS Inc. The research examined the UAV's wing and center bodies independently and separately. 3-D models were used for the analyses of the center body, while 2-D models were used for the wing-body analyses. The transition flow and submerged methods were taken into consideration in obtaining the impact load that a body experiences when transitioning into water. Because it was substantiated using experimental results from prior studies, the transient-time analysis-based transition technique was shown to be reliable. The steady-state analysis of the submerged flow method can be used to quickly comprehend the pressure and velocity distribution over a body immersed in or entering the water. However, because it fails to account for the water's initial acceleration upon entry, the steady-state simulation underestimates the drag force. The submerged flow method's findings indicate that a sharp nose centre body diminishes drag more successfully. The transition method evaluations for the UAV slender body reveal controllable drag and impact forces. Furthermore, the study demonstrates that wedge-shaped leading edges for the wing-body reduce impact but may not be optimal when considering airlift. As a result, this research provides useful data for air-sea UAV structural design and movement conditions.

Keywords Air-sea unmanned aerial vehicle · Transition method · Submerged flow method · Water entry · Finite volume method · Drag force

1 Introduction

Unmanned aerial systems have received more worldwide interest in recent years. The term "Unmanned Aerial System" (UAS) refers to the complete set of components, including ground control, supporting technology, communications, etc., that enable an unmanned aerial vehicle (UAV) to function [1]. Consequently, a UAV is a part of a UAS. It is a remotely flown aircraft without any occupants on board. The Global Hawk, Drones and the MQ-9 Reaper are a few examples of UAVs. The global market for UAVs has shown tremendous expansion. With a predicted compound annual growth rate (CAGR) of 7.9% from 2022 to 2027, the market for unmanned aerial vehicles was estimated to be worth USD 26.2 billion in 2022, and USD 38.3 billion by 2027 [2, 3]. Geographically, the worldwide UAV market is dominated

✉ Omolayo M. Ikumapayi
ikumapayi.omolayo@abuad.edu.ng

¹ Department of Mechanical Engineering, University of North Dakota, Grand Forks, ND, USA

² Department of Mechanical Engineering, Faculty of Technology, University of Ibadan, Ibadan 200005, Nigeria

³ Department of Mechanical and Mechatronics Engineering, Afe Babalola University, Ado Ekiti 360101, Nigeria

⁴ Department of Mechanical and Industrial Engineering Technology, University of Johannesburg, DFC, Johannesburg 2092, South Africa

⁵ Department of Mechanical and Construction Engineering, Faculty of Engineering and Environment, Northumbria University, Newcastle NE7 7XA, UK

by North America, with the United States accounting for the greatest share. As of 2021, there were 865,607 drones registered with the Federal Aviation Administration, and about 260,000 remote pilots that have received certification [4]. UAVs are now well-known throughout the modern world, due to their enormous possibilities and applications. UAVs are used in a number of industries, such as quarrying for the purpose of mineral exploration, public safety for the purpose of tracking down missing people or suspects, agriculture for the purpose of monitoring farmland and crop spraying, and the military for the purpose of enabling specific high-risk missions.

The Air-Sea UAV has a special application even though UAVs are typically only built for use in the air. The Air-Sea UAV can function both above and below water. It is intended to be able to fly, swoop down into the water, and ply the surface of the water while submerged. The high impact force that is felt when it tries to break through a water free surface presents a significant difficulty during the rapid transition from air to water. The likelihood of component failure and structural damage correspondingly rises. The development of thin jets (spray), large free surface deformation, air entrainment, and flow separation are all aspects of this flow problem's complexity. Henceforth, it is essential for the UAV's design to understand the accelerations and forces involved in this transition.

Since more than a century ago, academics have been interested in water entry problems and have conducted numerous experimental, analytical, and numerical studies. Worthington and Cole [5, 6] arguably are responsible for the earliest relevant work, which was completed in 1897. They looked at splashes and offered a variety of high-speed images. Subsequently water entry problems were extensively studied in relation to naval engineering. There are basically two research fields in water entry physics: research that focus on cavity formation and others with emphasis on impact force. Von Karman [7] proposed the first analytical approach for handling impact force caused by water entry in 1929. He established a mathematical equation using potential flow theory to calculate the impact load and suggested an additional mass approach. The fluid mass that moves with the body during impact makes up this additional mass. Contextually, the goal of his research was to improve existing knowledge on the hydrodynamics of seaplane landing. An improved version of Von Karman's approach was put out by Wagner [8]. The study considered free surface elevation by considering water entry process as a series. The author provided a formula for computing the two-dimensional wedge's instantaneous pressure distribution. Mackie [9] proposed a fully linear solution for a wedge-shaped body that enters the water.

Although theoretical studies have dominated the majority of the water entry research, experimental investigations have made a number of significant contributions to the subject.

In order to record the transition period, high-speed photography is frequently used in water entry experiments. Zhao et al. [10] conducted experimental performance tests on ship cross-sections. The experimental findings were put to use in a theoretical framework for a 2-D wedge. Tveitnes et al. [11] created a test rig that propels a wedge portion at a constant speed. The wetting factor and drag coefficient at varied deadrise angles were investigated using this technique. The deadrise angle is the inclination of a boat's bottom with respect to the horizontal plane. Nisewanger [12] investigated the pressure distribution on a 12-inch sphere during water entry experimentally. The pressure and drag coefficient were determined based of on penetration depth and time. Baldwin et al. [13] conducted similar experiments to Nisewanger [12], their results were in agreement. Shepard et al. [15] studied the impact of velocity and density, whereas May [14] focused on cavity growth while performing a drop test on a sphere. A body's impact force when it collides with water is primarily affected by the added fluid mass's rate of change in momentum, which may be connected to the rate of change of the body's wetted area [7, 8]. Impact forces are largely transient, and little research has been conducted in this area. May et al. [16] proposed a time-dependent model for resolving impact force to characterize projectile dynamics. Using the acceleration, velocity and gravity terms to dissect the impact force—Wang et al. [17], building on the work of May et al. [16], gave greater insight into the fleeting nature of the impact force. The hydrostatic and dynamic terms that make up the gravity term have varying values depending on the condition. Given the transient nature of impact forces, a transient-type solution would be the most appropriate for solving them.

Since Worthington's time [5, 6], researchers have been looking at the cavities that are created when a body enters water. One event which typically follows cavity formation is cavitation. Cavitation is a concept in which vapour cavities develop in a liquid when the static pressure in the fluid falls to a level underneath the vapour pressure. When a body hits a water surface with enough initial speed, an air cavity develops behind it [18]. A 1-inch steel sphere entering water was captured in high-speed motion images, according to May [14]. The May [14] study went into great depth about how cavities form. The initial splash is the consequence of water on the surface giving way to the entering body, and it marks the beginning of the water entrance cavity. As the body descends further, air is drawn in, and eventually the splash, which is at a level above the water's surface, forms a dome, sealing the surface. Hydrostatic forces then cause the hollow underneath to collapse, forming a pinch-off point. At the pinch-off sites, water jets are created, and they shoot through the upper cavity part and onto the water's surface. Images illustrating this process were also provided by several studies [14, 17, 18]. In attempting to simulate the effects of cavities forming and collapsing as a result of a high-speed projectile entering

the water, Lee et al. [19] put forward an analytical method. According to the model, the energy transmitted to the fluid to form the cavity and lost by drag on the projectile are both equivalent. The parameterization of cavities was taken into consideration by Plesset et al. [20] in the formation of water entry drag. By permitting two spheres to enter the water one after the other, Rasfan et al. [21] considered impact force mitigation. The hollow formed by the first sphere roughly lowered the force of impact on the second sphere by 78%. However, if the second sphere hits a collapsing cavity, the impact force is greater. When designing water-borne missile systems for the military, the cavity that forms during the water transition affects the item's path [14]. Important factors affecting cavitation in water entry include the projectile's characteristics (geometry, centre of mass, density and wettability), the angle of water entry and the velocity at the point of contact [18].

Because of the progress made in the application of numerical methods to impact force problems, more thorough studies of impact forces have been made possible. This has resulted in more reliable CFD methods that could address difficult water impact problems. It has been demonstrated that CFD methods based on Navier–Stokes equations (NSE) solutions for free surface flows are trustworthy. These NSE methods have the benefit of being generic, allowing for the simulation of intricacies of free surface deformation, flow separation, and the formation of jet-like flows. The difficulty in resolving the NSE for water entry is identifying the point where the surfaces of solid surfaces, water, and air converge. Free surface tracking methods, such as the Volume of Fluid (VOF) algorithm can be used to overcome this problem. Kleefsman et al. [22] explored the 2-D and 3-D water impact problems for wedges and cones, respectively, using the VOF method. The study offers convincing evidence in favour of the VOF method. Fairlie-Clarke et al. [23] also simulated the steady speed water entry of 2-D wedges for various deadrise angles using the VOF with finite volume discretization. Shen et al. [24] used Open FOAM's VOF and dynamic mesh method to simulate the entry of water and report the distribution of the sphere's forces and displacement. Finite volume method (FVM) on ANSYS CFX was used by Abraham et al. [5] in investigating the impact force experienced by a sphere. There have also been other CFD approaches used. Zhu et al. [25] tracked the free surface utilising the Constrained Interpolation Method in order to investigate the water entry and exit of horizontal cylinders. The impact force distribution for water entry at consistent velocity free fall was observed. Using the level set method, Zhang et al. [26] predicted the cylinder's slamming coefficient at water entry. The method and the experimental findings were discovered to be in excellent correlation. Aquelet et al. [18] used the Finite Element Method (FEM) along with the Arbitrary Lagrangian Eulerian (ALE) formulation to simulate

water entry for wedges [27]. Wagner's [8] theoretical findings were contrasted with the force and pressure gradient that were measured. Maruzewski et al. examined a sphere striking water using Smoothed Particle Hydrodynamics (SPH), a meshless method. Yan et al. [29] investigated the water entry forces of an autonomous unmanned vehicle (AUV) using both computational and experimental methods. A FEM and SPH formulation's merged predictions and experimental findings showed excellent accord. Serge [30] reviewed the dynamic behavior of water entry and how they relate to hull slamming in great detail. The study looked at a variety of methods that had been used in water entry problems over the years.

The effectiveness of a UAV transitioning from air to water was numerically studied in this research. The authors examined the forces and accelerations that the wing and fuselage parts of the UAV encountered during the change. Utilizing CFD, a numerical strategy that can handle the water entry process was established. This study's simulations were all run using the commercial software FLUENT from the holding company ANSYS Inc. The effectiveness of the designed numerical method was shown by contrasting the simulated transition of a sphere with experimental results from other scientists. The study considered the UAV's wing body and centre body separately and independently to simplify the evaluation. Wing body investigations were conducted using 2-D models, whereas 3-D models were used. Wing body investigations were conducted using 2-D models, while centre body analyses were conducted using 3-D models. used for the centre body analyses.

2 Methodology

This section describes the computational set-up developed to simulate the air-to-water transition problem for a UAV. This is accomplished by simulating a spherical aluminum body using CFD. The goal is to create a reliable simulation system that can correctly resolve the flow dynamics that take place as an object transitions from air to water. As a result, the validation study provides a solid foundation for this work's subsequent simulation.

2.1 Validation study

The present study aims to evaluate the reliability of a simulation approach by comparing its results with those obtained from an experimental investigation conducted by Nisewanger [12]. Nisewanger's investigation involved analyzing the pressure distribution on a 0.305 m (12 in.) aluminum sphere as it entered water at a constant velocity of 7.163 m/s (23.5 fps). Baldwin and Steves [25] also performed similar research

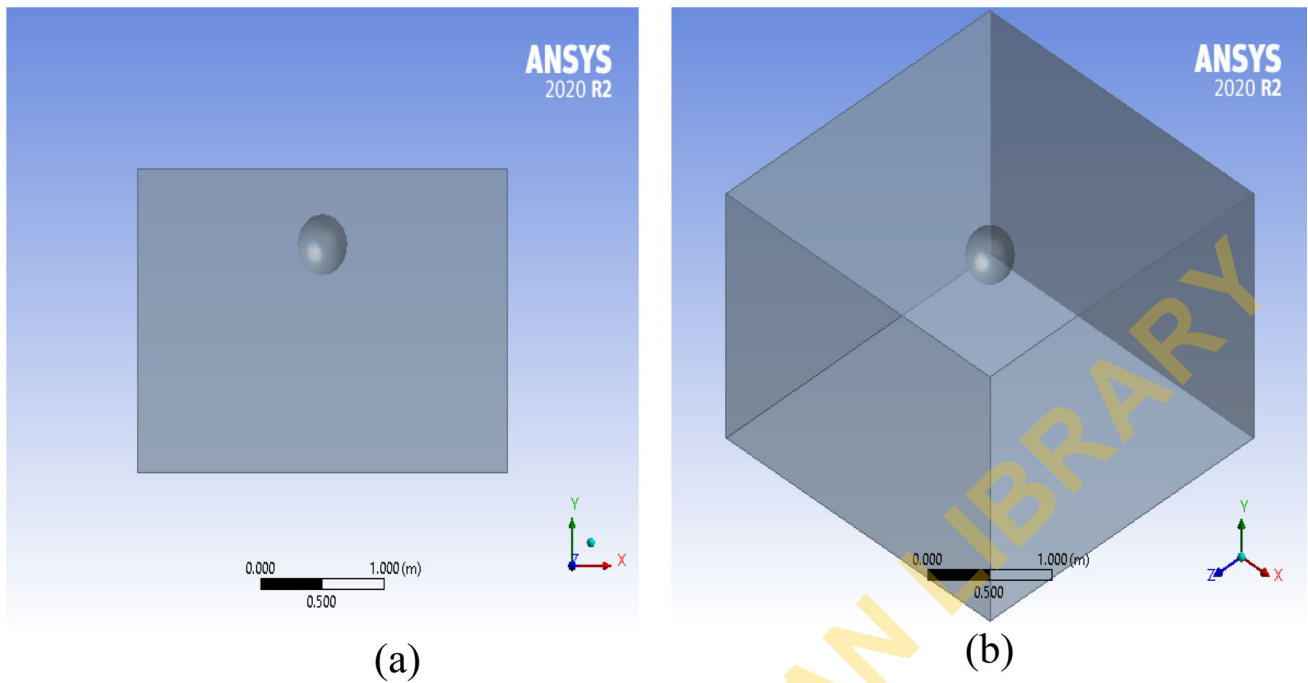


Fig. 1 a Domain geometry side view of sphere water entry b Domain geometry of sphere water entry

and obtained results that were consistent with those of Nisewanger [12]. Furthermore, Pengyao et al. [31] carried out a numerical validation study using the STAR-CCM+ commercial software. Figure 1 shows the computational domain used in the study. To simulate the sphere's transition from air to water, a time-dependent realizable k - ε turbulence model with a scalable wall function was employed. To ensure an accurate and realistic solution, appropriate spacing was maintained between the sphere and the side and bottom surfaces during the mesh generation process. The dynamic mesh technique was employed specifically for generating meshes around the sphere within the computational domain. Given that it only interacts with the air medium, the upper layer was chosen as a pressure outlet with a volume fraction of one for air to water. The velocity and pressure fields were coupled in the solution scheme using the semi-implicit method for pressure-linked equations (SIMPLE), which is a pressure-based solver. The volume fraction of air to water was also solved using the volume of Fluid (VOF) method. In this computation, a residual value of $1e-06$ and a time step of $1e-05$ s were used.

3 Governing Equations:

For this fluid–solid coupling problem, the RANS k - ε turbulent model was used.

$$\frac{\partial u_i}{\partial x_i} = 0 \quad (1)$$

$$\frac{\partial u_i}{\partial t} + u_j \frac{\partial u_i}{\partial x_j} = -\frac{1}{\rho} \frac{\partial p}{\partial x_i} + g_i + \frac{\partial \tau_{ij}}{\partial x_j} \quad (2)$$

k - ε model:

$$\frac{\partial k}{\partial t} + u_j \frac{\partial k}{\partial x_j} = \frac{\partial}{\partial x_j} \left[\left(\frac{v_t}{\sigma_k} + v \right) \frac{\partial k}{\partial x_j} \right] + G - \varepsilon \quad (3)$$

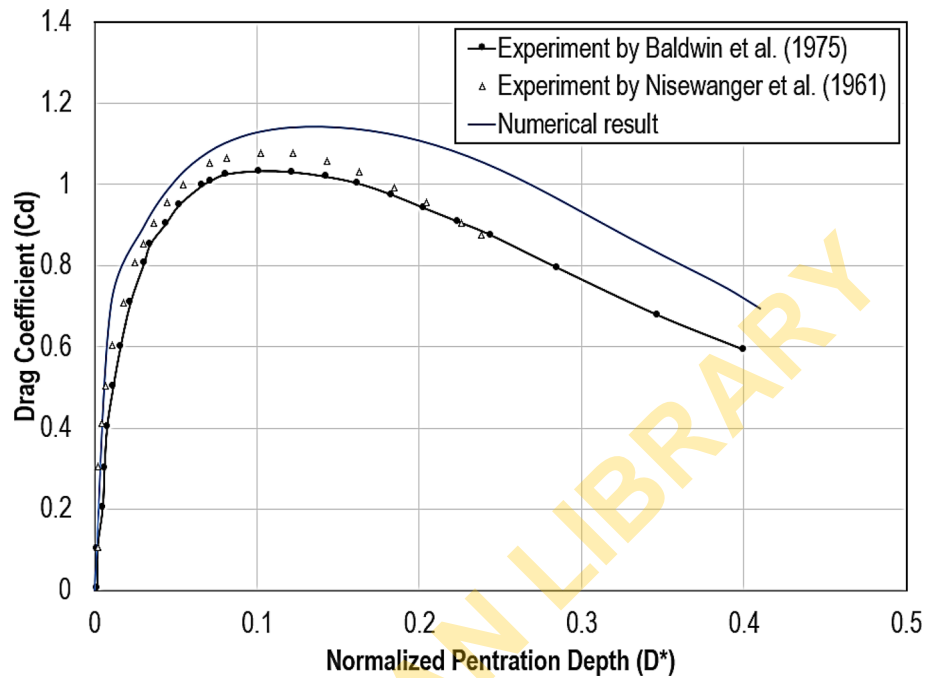
$$\frac{\partial \varepsilon}{\partial t} + u_j \frac{\partial \varepsilon}{\partial x_j} = \frac{\partial}{\partial x_j} \left[\left(\frac{v_t}{\sigma_\varepsilon} + v \right) \frac{\partial \varepsilon}{\partial x_j} \right] + C_{1\varepsilon} \frac{\varepsilon}{k} G - C_{2\varepsilon} \frac{\varepsilon^2}{k} \quad (4)$$

where $\tau_{ij} = 2(v + C_d(k^2/\varepsilon))\sigma_{ij} - (2/3)k\delta_{ij}$, $\sigma_{ij} = (1/2)((\partial u_i/\partial x_j) + (\partial u_j/\partial x_i))$, $v_t = C_d(k^2/\varepsilon)$, $G = 2v_t\sigma_{ij}(\partial u_i/\partial x_j)$, $C_d = 0.09$, $C_{1\varepsilon} = 1.44$, $C_{2\varepsilon} = 1.92$, $\sigma_\varepsilon = 1.3$, $\sigma_k = 1.0$.

ε is the turbulent dissipation rate, k is the turbulent kinetic energy, σ_{ij} is the rate of the strain tensor, v_t is eddy viscosity, u_i velocity vector of the mean flow, δ_{ij} is the Kronecker delta function, g_i is the i th component of the gravitational acceleration, ρ is the fluid density, p is the pressure of the mean flow. The simulation outcomes are juxtaposed with the experimental findings of Nisewanger [12] and Baldwin and Steves [13], as presented in Fig. 2. The total vertical force represented by the drag coefficient C_D is plotted against the normalized penetration depth (D^*).

$$C_D = \frac{D}{\frac{1}{2}\rho_\infty V^2 A} \quad (5)$$

Fig. 2 Drag Coefficient comparison of sphere at water entry



$$D^* = D_p/R \quad (6)$$

The comparison conducted revealed that the simulated drag coefficient in this study correlates well with experimental data, with a marginal deviation. The simulated peak drag exceeded the experimental value by 5%. Therefore, it can be inferred that the simulation approach employed in this study is adept at modeling objects that undergo transition from air to water. Figure 3 depicts the contour plot of the sphere in transition.

3.1 Simulation of air-sea UAV

The validated model approach is used to simulate the Air-Sea UAV's transition from the air to the sea. The UAV was split into two distinct body sections to make analysis easier.

1. *Center body*: The center body sometimes referred to as fuselage, bears most of the UAV's weight and functions as a structural link between the wing and tail assembly. It is also responsible for the majority of the UAV's drag.
2. *Wing body*: This section is mainly a stack of airfoils linked to the fuselage's side. They act as the main lifting surface that keeps the UAV flying.

3.2 CFD setup

Two general instances were simulated: a fully submerged body and a vertically descending body transitioning from air

to water (refer to Fig. 4). The fully submerged body simulation was conducted under steady-state conditions, while the latter employed transient-state conditions. A submerged body's steady-state analysis allows for a quick understanding of the velocity and pressure distribution over the transitioning or submerged body. Moreover, the steady-state simulation does not account for the fluid's initial acceleration, which can substantially increase the initial force of impact on the vehicle, particularly in areas with blunt edges. While the transition method was used to simulate the wedged leading edge, elliptical leading edge, and UAV slender body, the submerged flow method was used to model the NACA 0012, conical nose model, elliptical nose model, and the wedged NACA airfoil.

3.3 Domain geometry

Three distinct designs were examined for the centre body in this study: a slender body with lines resembling a pre-selected UAV, an axi-symmetric body with an elliptical nose, and an axi-symmetric body with a conical nose. We also looked at elliptical leading edge and wedged leading edge models, two-dimensional (2-D) models that are planar and describe the longitudinal section of the axially symmetric bodies. The NACA 0012 airfoil and a wedged-type NACA 0012 airfoil were used to evaluate the performance of the wing body. The elliptical leading-edge design has a major length of 2.06 m, compared to 2.35 m for the wedge shape. The elliptical nose centre body had an ellipse ratio of 3.2:1, whereas the conical nose centre body had a half angle of 15°. The NACA 0012's coordinates were found in the airfoil online database [32], and the wedge airfoil's leading edge had a half angle of 15°.

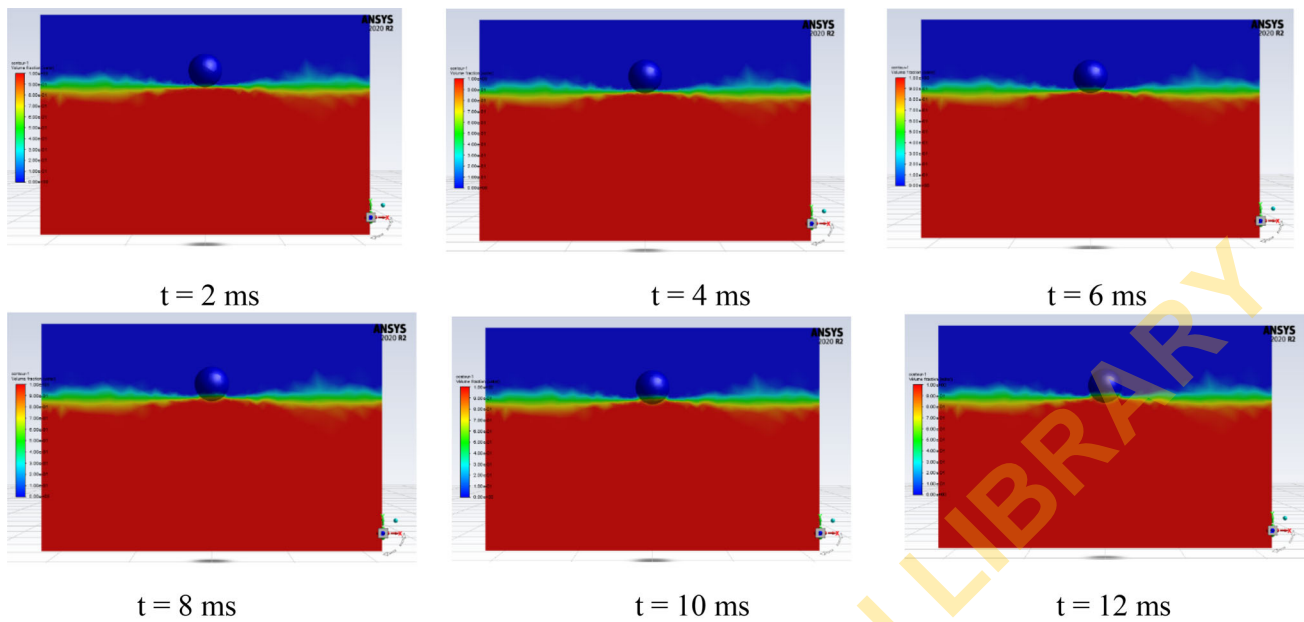
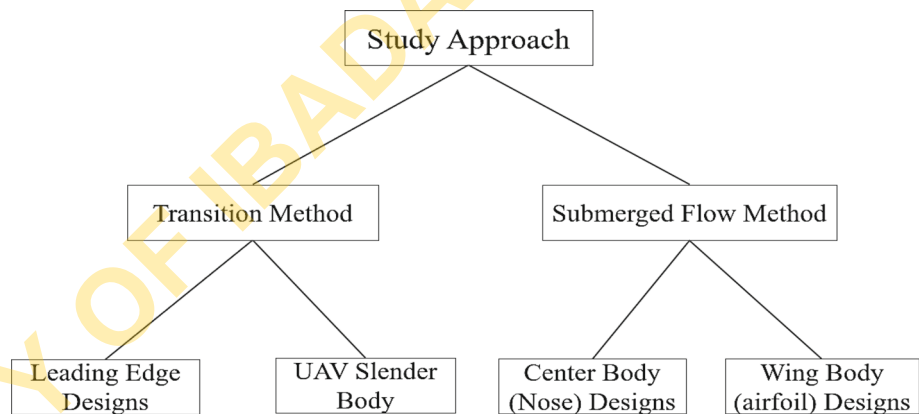


Fig. 3 Ball position at different time instance

Fig. 4 Study Approach Chart



Figures 4, 5, and 6 provide thorough illustrations of these models in more detail.

3.4 Meshing

For the simulation, the Mesh software package from ANSYS was used.

- I. *Conical-Nose-Center-Body*: The average mesh element type in the fluid domain away from the body is $4e-01$ m, and it is basically consistent. A sphere of impact was established around the body using an inflation first layer height of $2e-06$ m and an element size of $3e-02$ m to capture the relevant information of the fluid domain close to the body. 5,65,194 nodes and 2,993,421 elements made up the final mesh.
- II. *Elliptical-Nose-Center-Body*: The computational mesh used in this simulation consists of elements with

sizes of $4e-01$ m away from the body, $3e-02$ m close to the body, and $2e-06$ m for the first layer height in the inflation layer. The mesh has a total of 334,709 nodes, and 756,021 elements. It is largely uniform.

- III. *UAV-Slender-Body*: The mesh used had two interior boundary points. A coarser mesh with an element size of $1e-01$ m, an inflation layer with a first height of $1e-02$ m and a face size of $2e-02$ m was used for the region surrounding the slender body. The mesh was structured with an average element size of $3e-01$ m in the area away from the slender body. 1,916,361 elements and 2,883,509 nodes make up the mesh. The element sizes were selected to avoid negative volumes during mesh changes while being fine enough to capture significant features. Mesh types that are unstructured and irregular are considered. The adopted element types are listed in Table 1.

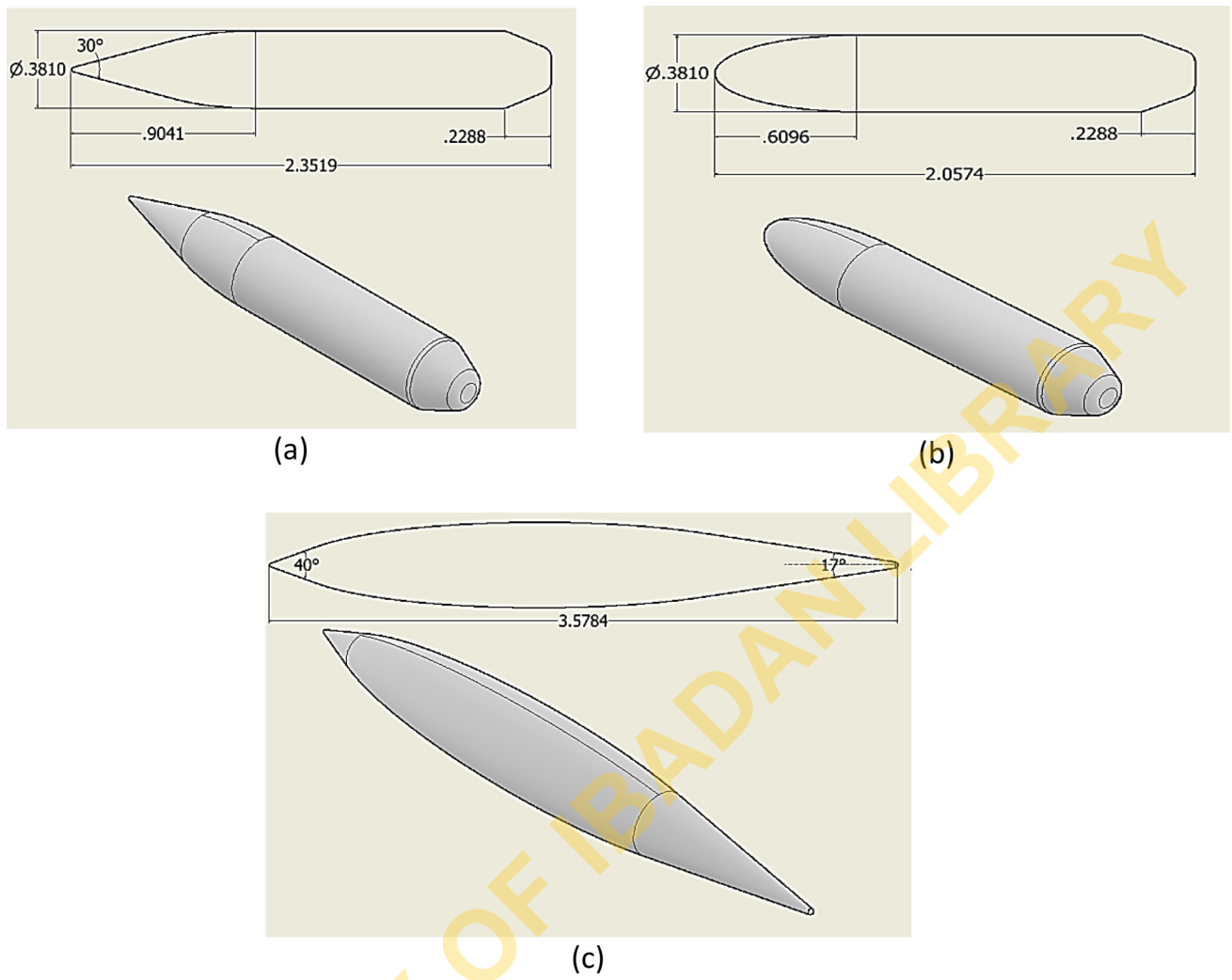


Fig. 5 The model geometries **a** conical nose, **b** elliptical nose, and **c** slender body

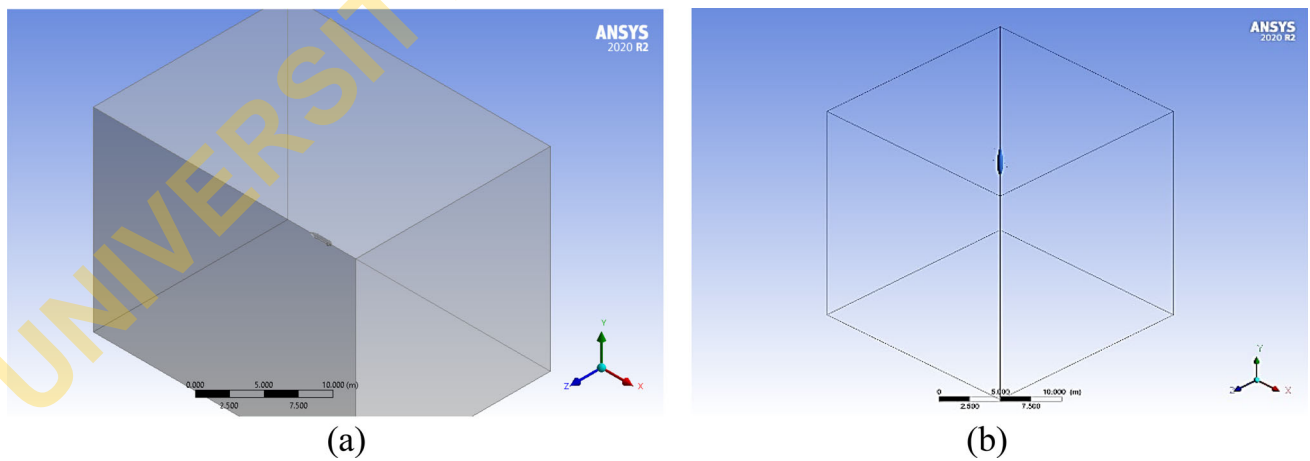


Fig. 6 Fluid domain **a** Submerged case **b** Transition case

Table 1 Mesh characteristics of UAV slender body

Parameter	Method/value
Element order	Quadratic
Mesh type	Unstructured
Volume	Tetrahedral
Advanced size function	Proximity and curvature
Growth rate	1.1
Relevance center	Fine
Adaptive Sizing	No

- IV. *Wedge-Leading-Edge*: The element size in this mesh is $4e-02$ m. The rigid body's edges are divided by 40 and have an inflation layer first height of $3e-03$ m. This mesh is considered fine, with 312,461 nodes and 159,814 elements.
- V. *Elliptical-Leading-Edge*: The element size for this mesh is $4e-02$ m, with an inflation layer first height of $3e-03$ m and edge sizing accomplished by dividing into 40 parts. The mesh has 309,670 elements and 626,324 nodes in total.
- VI. *NACA-0012-Airfoil*: The airfoil was represented by a very fine mesh, with a boundary layer having a first height of $1e-06$ m. The mesh size was $4e-03$ m for the area closest to the airfoil and $1e-01$ m for the area farther away. This unstructured mesh had a total of 325,500 elements and 177,315 nodes, and it was relatively uniform.
- VII. *Wedge-NACA-0012-Airfoil*: This mesh is similar to that of the above-mentioned airfoil, but it has a mesh size of $3e-03$ m close to the airfoil. The mesh has 448,305 elements and 251,719 nodes and is unstructured with a primarily uniform distribution.

The mesh properties are given in Table 1.

3.5 Solver setup and boundary conditions

The boundary and operating conditions were quite similar for simulations of fully submerged bodies and bodies undergoing transition. As previously mentioned, dynamic meshes were used for time-dependent cases, while fixed meshes were used for fully submerged situation. In both instances, a residual value of $1e-06$ was used.

3.5.1 Transition case

The time-dependent air-to-water transition method was used to simulate the slender body as well as the two-dimensional (2-D) models of the center body (elliptical leading edge and wedge leading edge). The pressure outlet was set as the top

surface, while the other surfaces within the domain were set as walls, as illustrated in Fig. 6b. The 6061 Aluminum alloy is the default material for the rigid body, which is set to as a wall. To define these rigid bodies which are irregular in shape, Autodesk INVENTOR was used to determine parameters such as mass, area moment of inertia, and center of gravity.

3.5.2 Submerged case

The steady-state submerged flow method was used to simulate the wing body and the 3-D models of the center body. The right and left surfaces were set as pressure outlet and pressure inlet, respectively, while the remaining faces were set to walls. The domain was designed to be sufficiently large to account for any computational instability. By adjusting the total pressure and gauge pressure using Eq. (7), the flow rate of the water was predefined. The semi-implicit method for the pressure-linked equation (SIMPLE) with second order upwind spatial discretization was chosen as the solution approach (Fig. 7).

$$P_0 = P_s + \frac{1}{2}\rho V^2. \quad (7)$$

4 Result and discussion

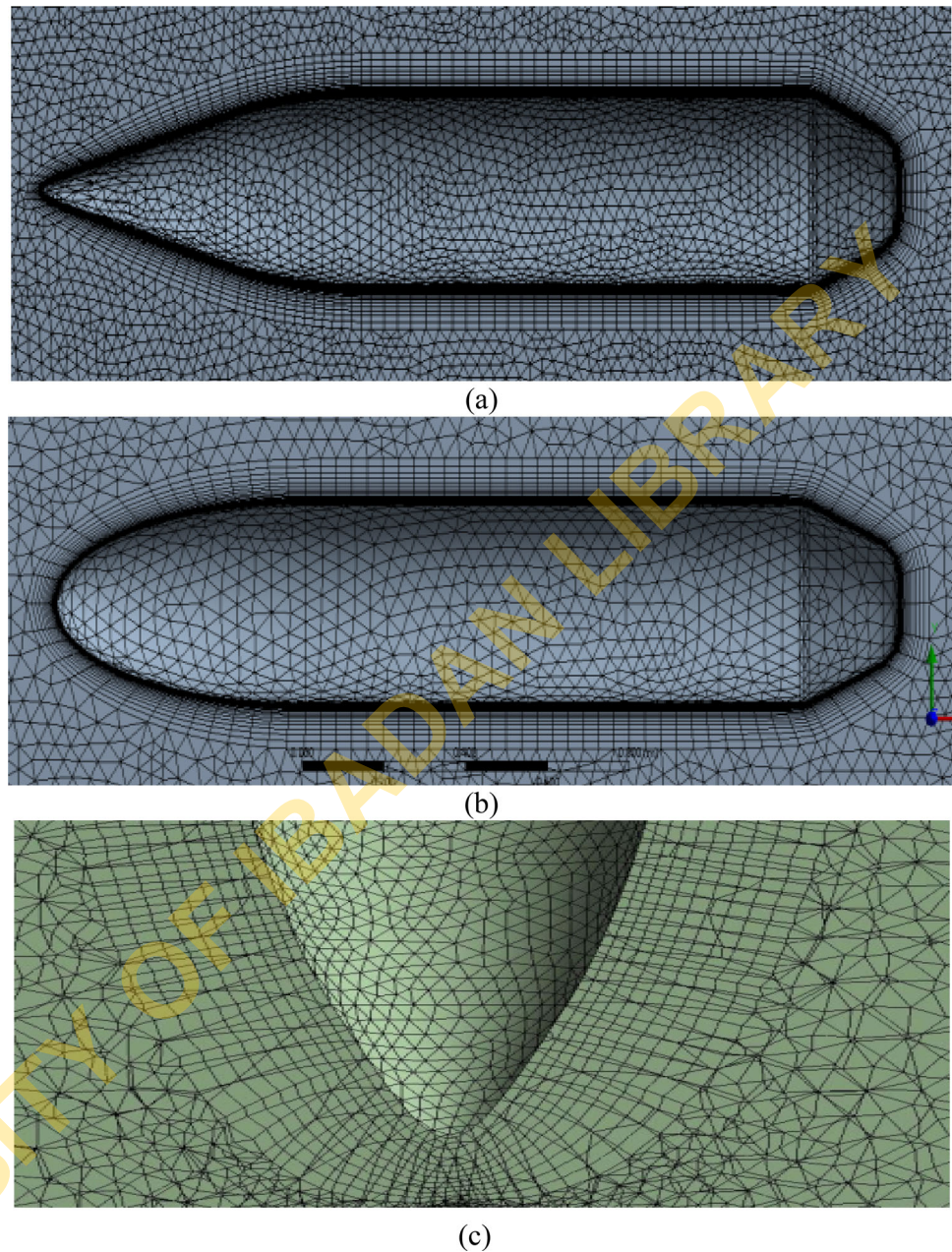
4.1 Transition case

The model was placed 0.096 m from the water's surface and initialised with a starting velocity of 50 m/s. For the modelling, a time step granularity of $2e-05$ s was used.

4.1.1 Transition case for leading edge design

Figure 8 shows the drag coefficient, also referred to as the impact force coefficient, for the elliptical and wedge leading edges. The water is initially at rest and must accelerate quickly upon contact with the leading edge, which affects the impact force. More water must be sharply accelerated by the elliptical leading edge, which causes the initial impact pressure and force to significantly increase. The wedge-shaped leading edge, on the other hand, has a smaller frontal area and requires less fluid to be abruptly accelerated. The drag coefficient plot illustrates this, demonstrating that the drag coefficient for the wedge shape is roughly one-fourth that for the elliptical shape. The wedge leading edge's drag coefficient plot has two peaks, the first connected to the water's abrupt acceleration as the wedge breaks the surface and the second to the area of the wedge shape increasing as it enters the water. Figures 9 and 10, respectively, display the two shapes' velocity and acceleration profiles. The

Fig. 7 The zoomed-in mesh grid
a conical nose, **b** elliptical nose,
c slender body, **d** airfoil,
e wedged airfoil



water is initially accelerated upon contact with the elliptical leading edge, which causes the initial abrupt decrease in velocity for the leading edge. The acceleration slows down due to the development of the flow field around the body. Due to its smaller size, the wedge-shaped leading edge requires less water to be abruptly accelerated, but the acceleration increases as more surface area moves into the water.

The static pressure distributions around the bodies when they were being submerged in water are shown in Figs. 11 and 12. The two plots have different scales. The body experiences a significant increase in pressure during the water entry, which causes the water to accelerate around the leading edge. Cavitation is the separation of water from the surface and the

formation of cavities as a result of a pressure drop caused by an increase in the velocity of the water on the surface. The blue line, which represents the pressure distribution around the body at impact, is followed by the orange line, which represents the pressure distribution at a normalised distance of about 0.04, and so on. Water has a cavitation pressure of 3.2 kPa at standard pressure and temperature. As a result, the areas on each line where pressure values are less than 0 Pa are where cavitation takes place on the body.

The positions of the models at various times during their transition into water are shown in Figs. 13 and 14. On the figures, the water region is depicted in red, and the air region is shown in blue. The elliptical leading edge is shown in

Fig. 7 continued

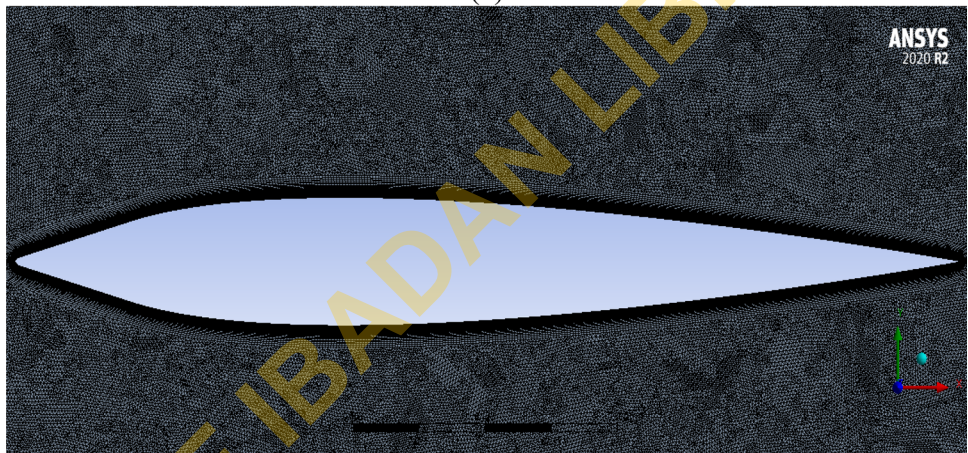
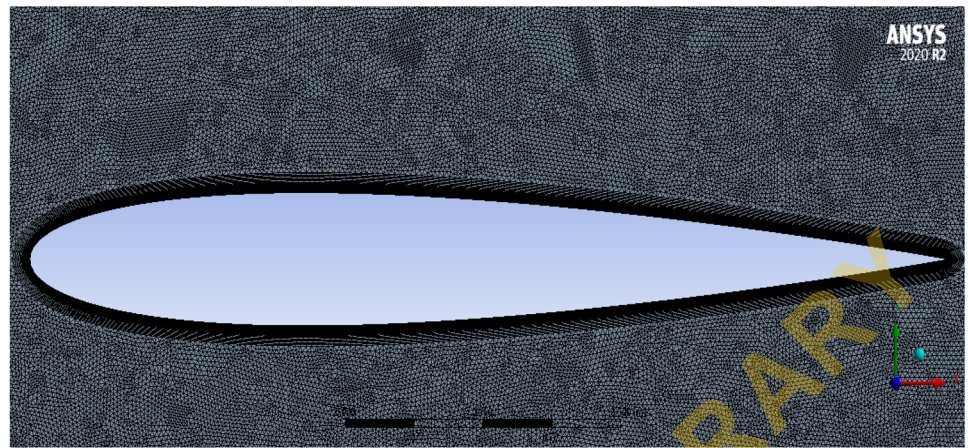


Fig. 8 Drag coefficient comparison on leading-edge designs

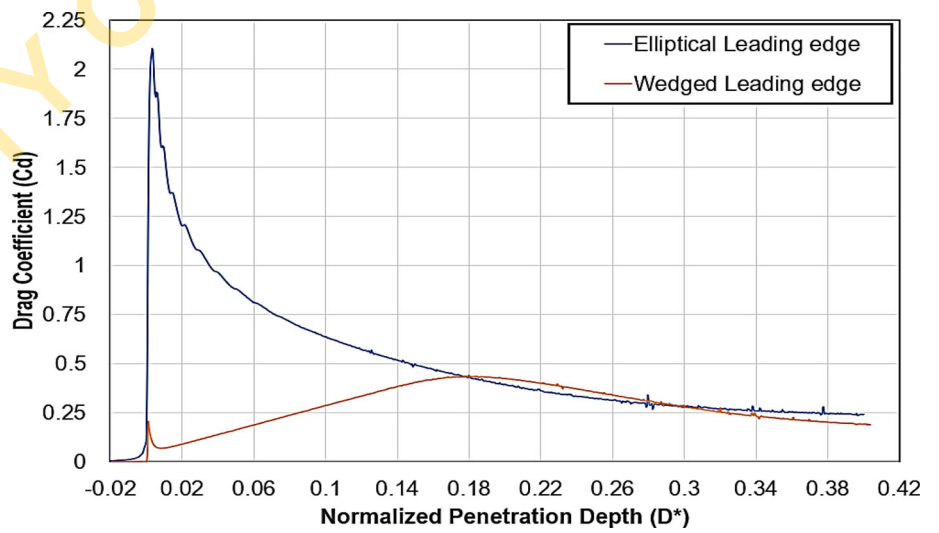


Fig. 9 Velocity profile plot

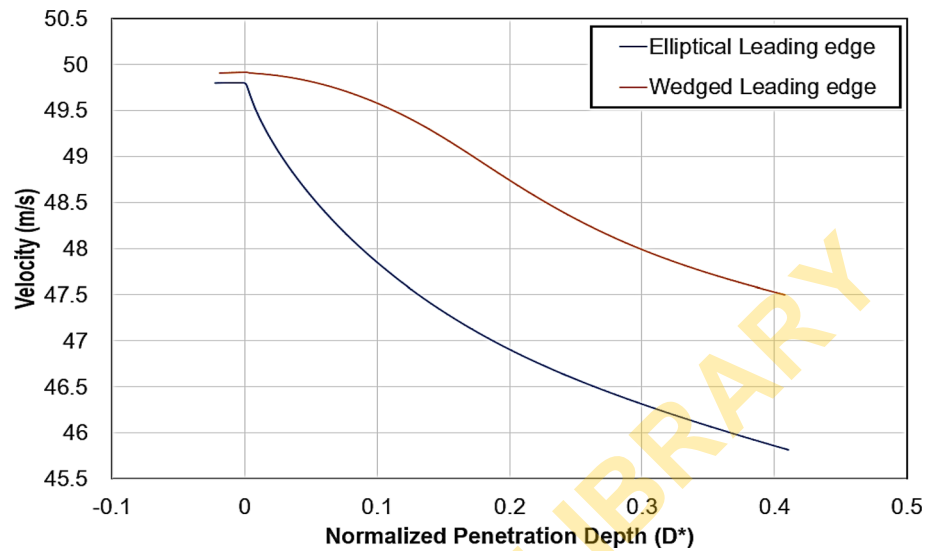


Fig. 10 Acceleration profile plot

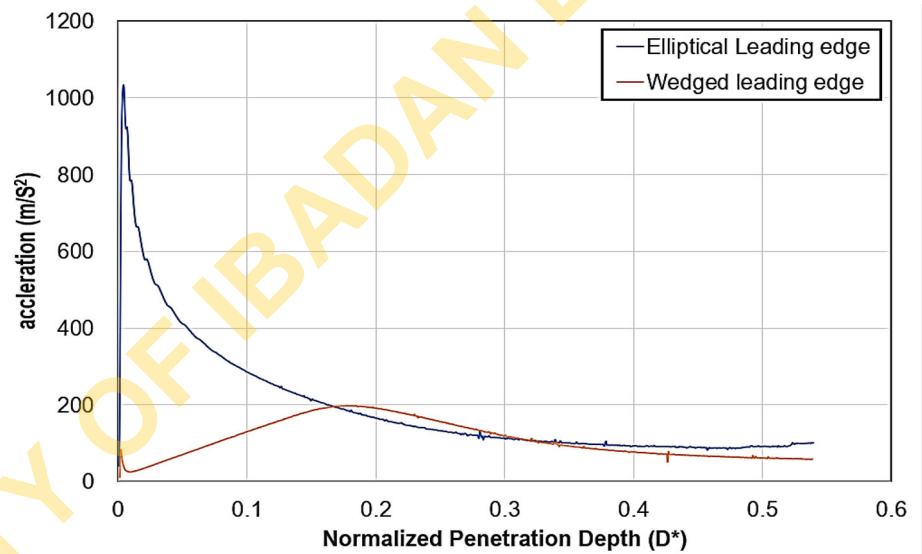


Fig. 11 Pressure distribution around the elliptical leading-edge model during water entry

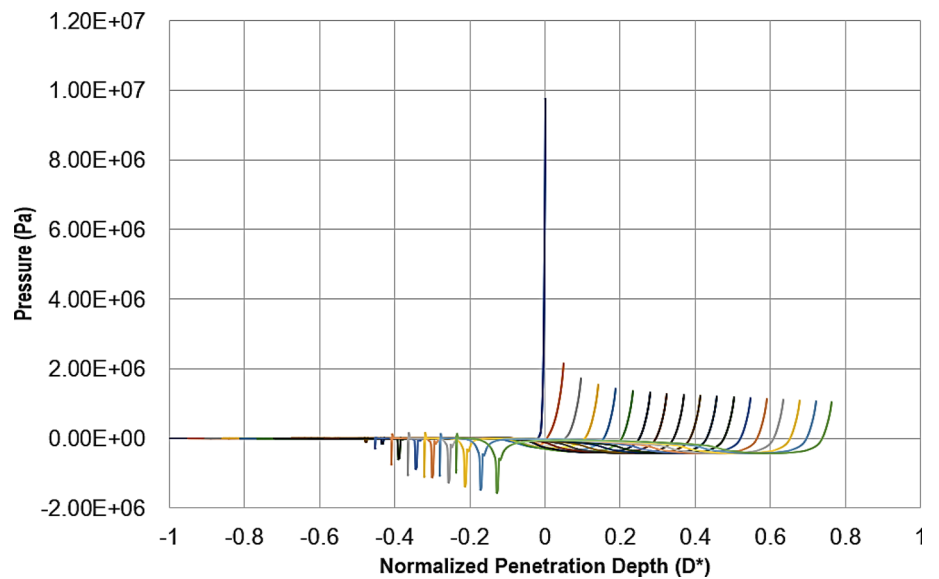


Fig. 12 Pressure distribution around the wedge leading edge model during water entry

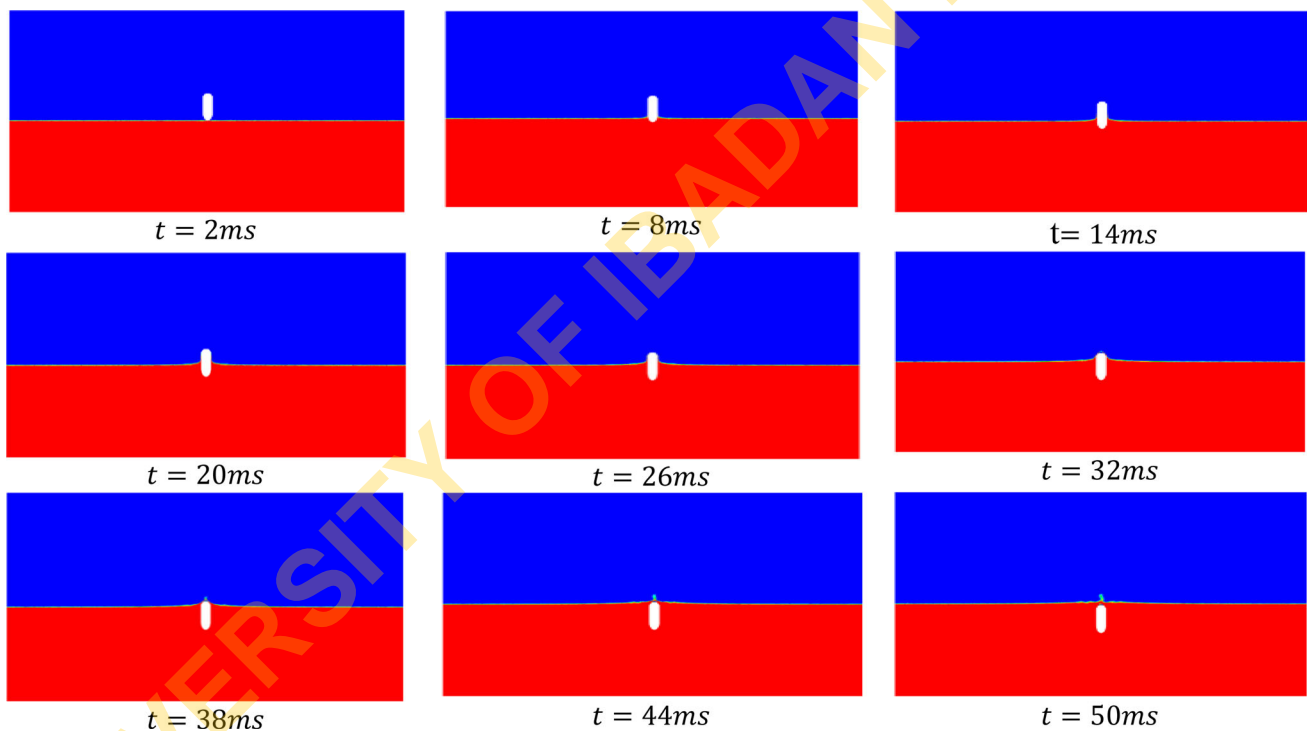
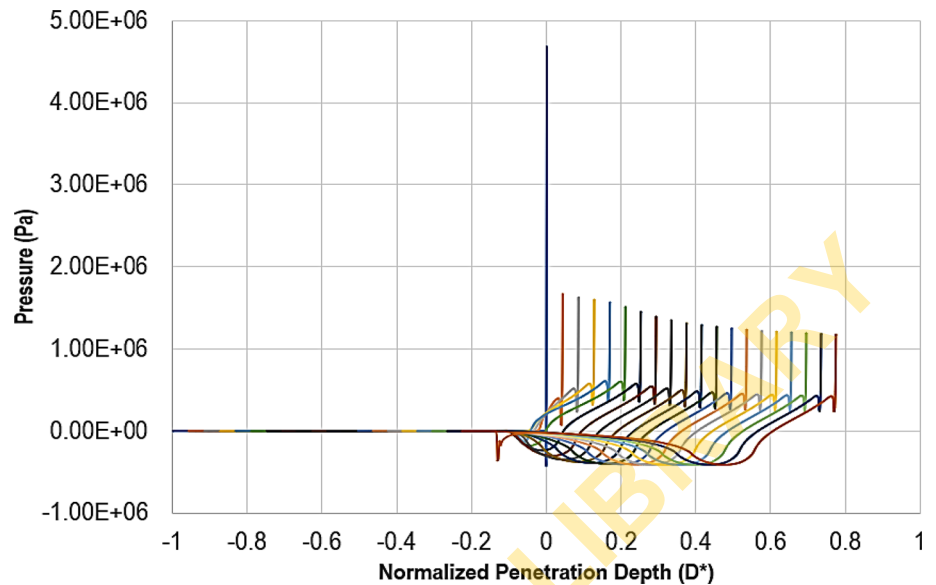


Fig. 13 Position of elliptical leading edge model at different time instants

Fig. 13 while the wedge-shaped leading edge is shown in Fig. 14.

4.1.2 UAV slender body

To replicate the shape of an actual UAV, a model with comparable contours was made. The body measures 3.58 m in length and has a conical nose with a 20-degree half-angle. The centre section, which has a maximum diameter of 4.88e-01 m

and is situated 1.536 m from the front, smoothly connects to the nose segment (refer to Fig. 5c). The mass of the model is estimated to be 988 kg. The drag coefficient, a dimensionless force that describes the amount of resistance a body experiences as it moves through a fluid, is shown in Fig. 15. The section with the largest diameter also falls within the plot's trough region.

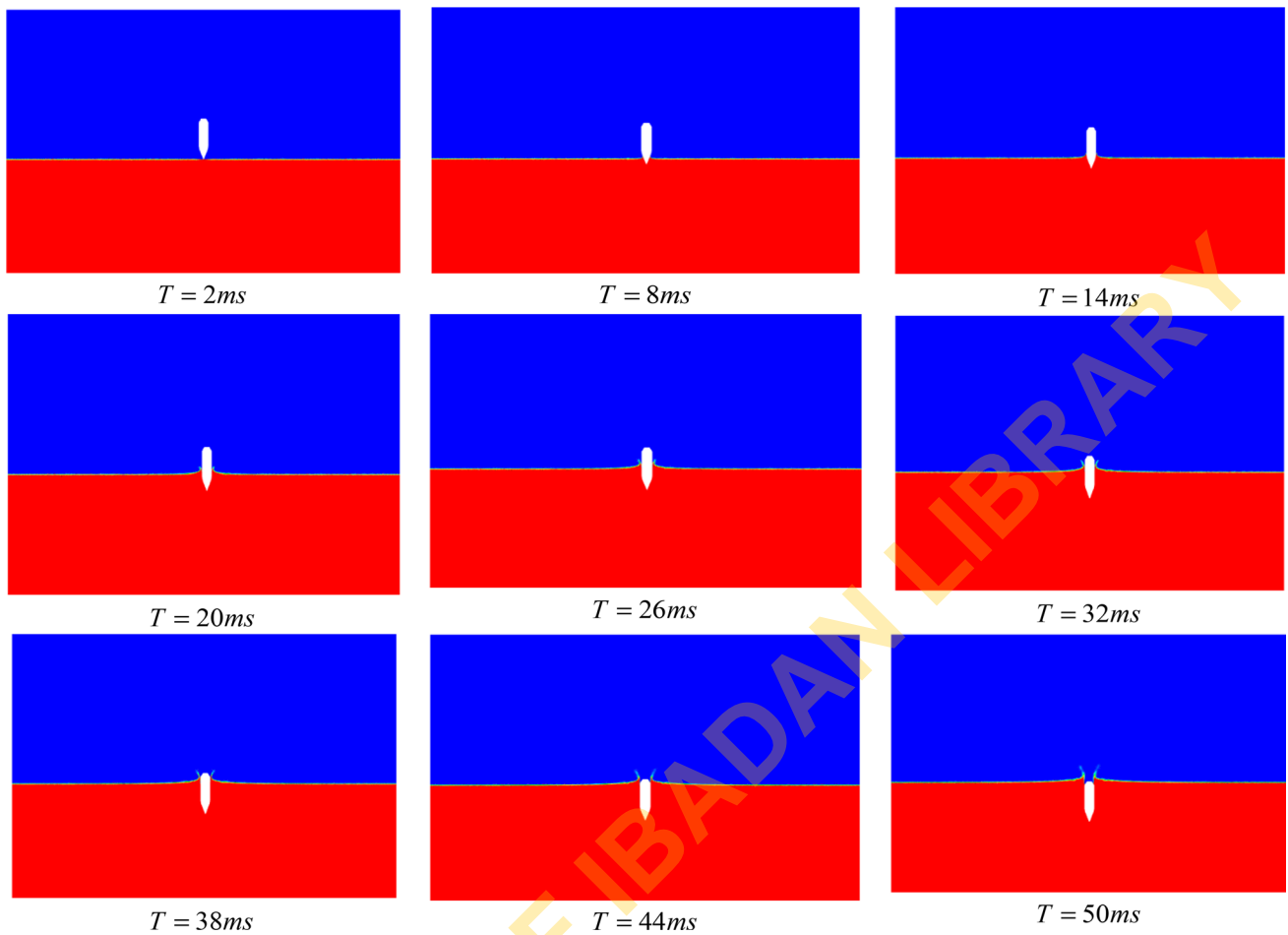


Fig. 14 Position of wedged leading edge model at different time instants

Fig. 15 Drag coefficient plot of UAV slender body

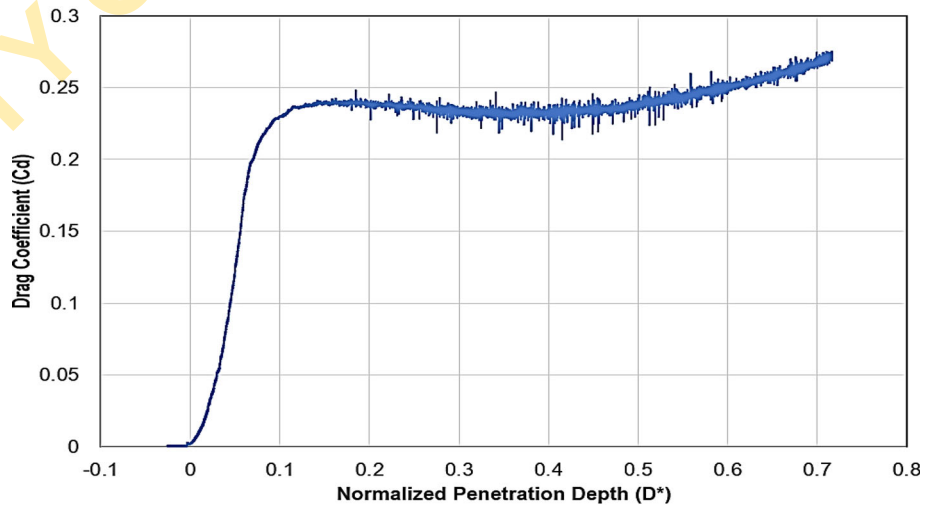


Fig. 16 Velocity profile as the slender body during the water-entry

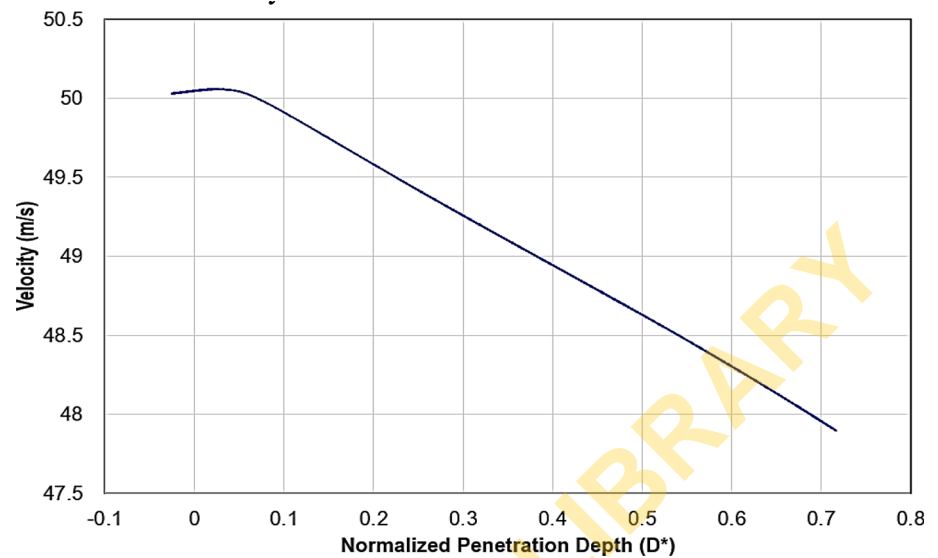
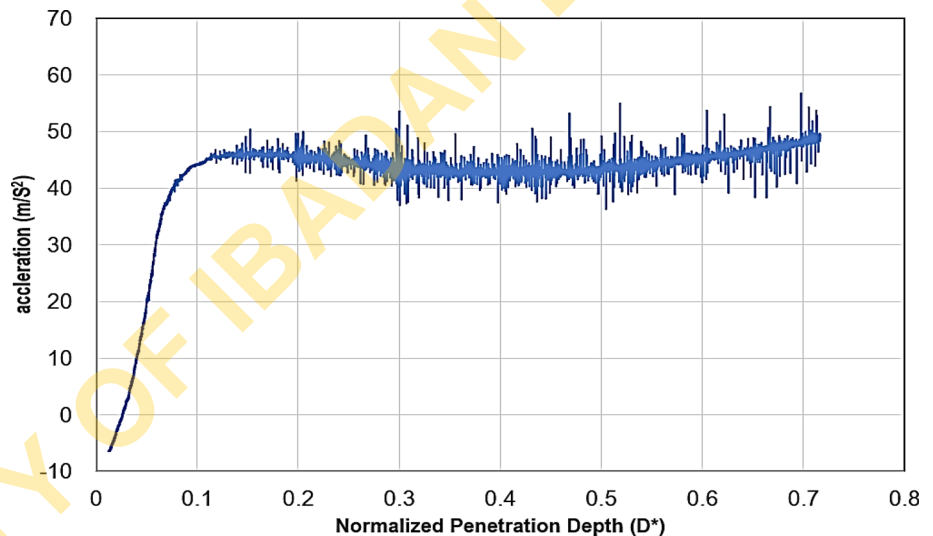


Fig. 17 Acceleration profile as the slender body during water-entry



The linear and downward-sloping velocity profile in Figs. 16 and 17 indicates that the body experiences a relatively constant acceleration. This behaviour is caused by the body's streamlined shape, which prevents abrupt changes in flow by ensuring a smooth transition from the conical nose to the midsection and finally to the end section.

Figures 18, 19, 20 provide more information about the UAV's slender body. The pressure distribution around the body as it enters the water is depicted in Fig. 18. The body's nose section experiences the highest pressure, and the middle region shows prominent cavitation.

4.2 Submerged flow case

True time-dependent water transition simulation development is a difficult task requiring substantial computational resources. Therefore, the initial investigation of the current

problem involved determining the immersed flow around a body and calculating the drag force based on the expected wetted area before cavitation. Water is separated from the body's surface at the point of cavitation, leaving it exposed to the atmosphere. The drag coefficient is determined using the atmospheric static pressure distribution that results from this point of cavitation to the end of the body that's exposed to the atmosphere. However, this approach does not take into account the water's sudden acceleration at the time of initial water entry.

4.2.1 Comparison of center body design

The pressure contour on surfaces with an elliptical nose and a conical nose are shown in Figs. 21 and 22, respectively. The pressure is highest at the tip of the nose, also known as the stagnation point. However, due to the slight deformation

Fig. 18 Pressure distribution around the UAV's slender body as it moves further in water

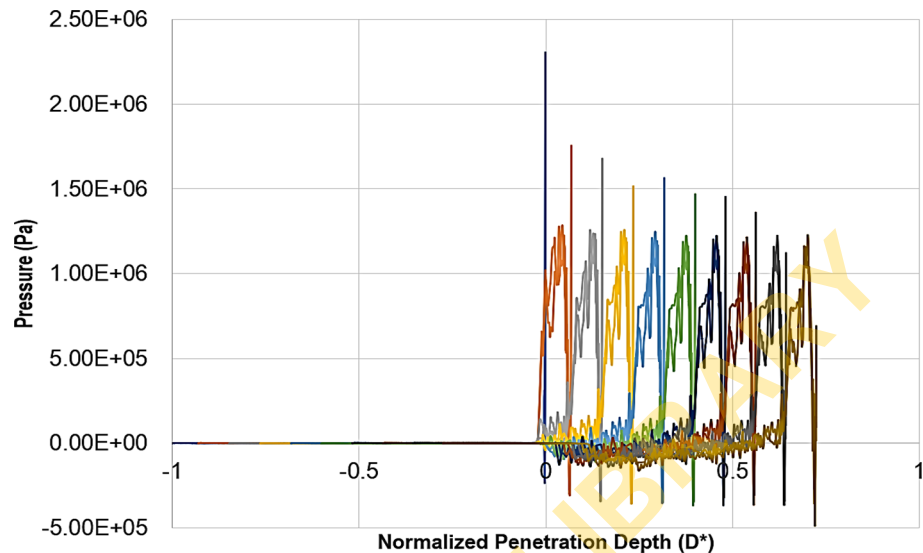
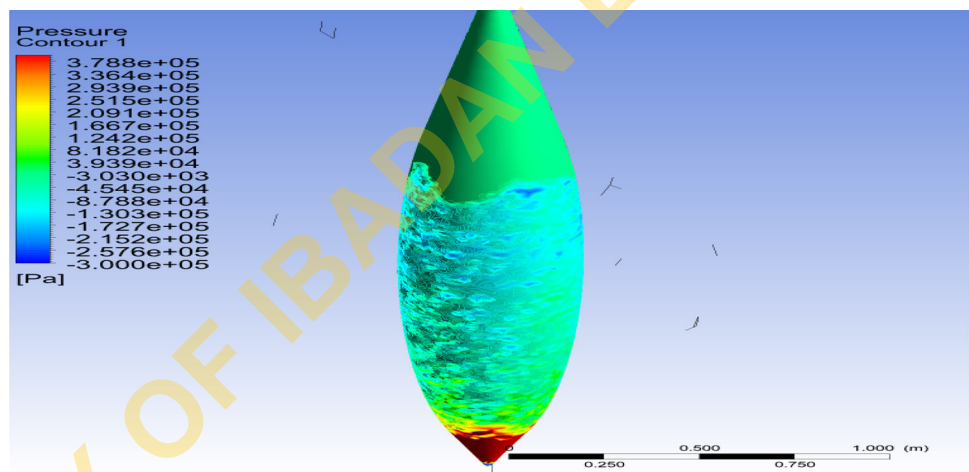


Fig. 19 Pressure Contour at a normalized depth of 0.72 (color spectrum limited to range $-3e05$ to $4e05$ Pa)



brought on by the meshing process, the values shown in the figures are not smoothly resolved around the curvature. Since a sharp nose tip rather than a curved one was created for the conical nose model, the flow diffuses quickly away from it. By carefully looking at the zoomed-in mesh in Fig. 7a and b, this can be seen. However, it is anticipated that the pressure on the coarse surface elements will be a good indicator of the model's overall curvature.

Figure 23 shows the dimensionless drag, also known as the drag coefficient, which is a useful measure of the amount of resistance a body encounters when moving through a fluid. The drag and drag coefficient were calculated using Eqs. 8 and 5, respectively.

$$D = \int_{y_1}^{y_2} P_s \cdot 2\pi y dy \quad (8)$$

The body length was used to plot the distribution of the drag coefficient. The pressure that is thought to exist

past the point of separation is atmospheric (101,325 kPa) as previously mentioned. Just prior to separation, the drag coefficients for the conical and elliptical leading edges were determined to be $1.05e-01$ and $1.29e-01$, respectively. The elliptical and conical nose centre bodies, respectively, had the largest dimensionless drag coefficients measured, measuring $1.4e-01$ and $1.7e-01$.

4.2.2 Comparison of wing body designs

Figures 24 and 25 display the pressure contours around two airfoils, the NACA 0012 symmetrical airfoil and the wedged leading-edge airfoil. These data show that although there is a smooth variation in pressure along the surface, the pressure at the leading edge is relatively high.

The drag coefficient distributions for the typical NACA 0012 airfoil and the wedge-shaped leading-edge airfoil are contrasted in Figs. 26 and 27. For both airfoils, the pressure rapidly decreases at the leading edge. The wedged airfoil

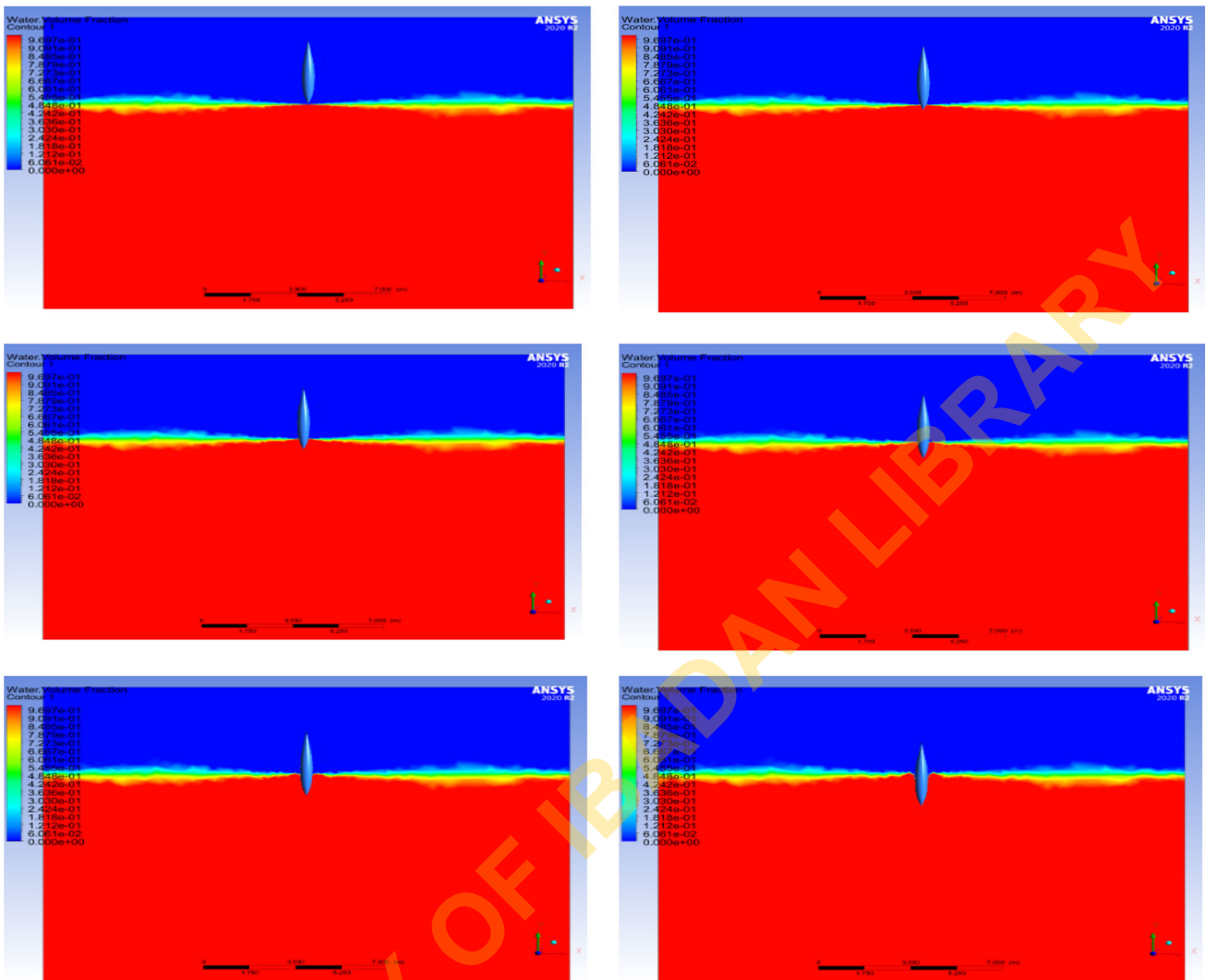


Fig. 20 Images of UAV slender body as it descends

Fig. 21 Pressure contour of elliptical nose model

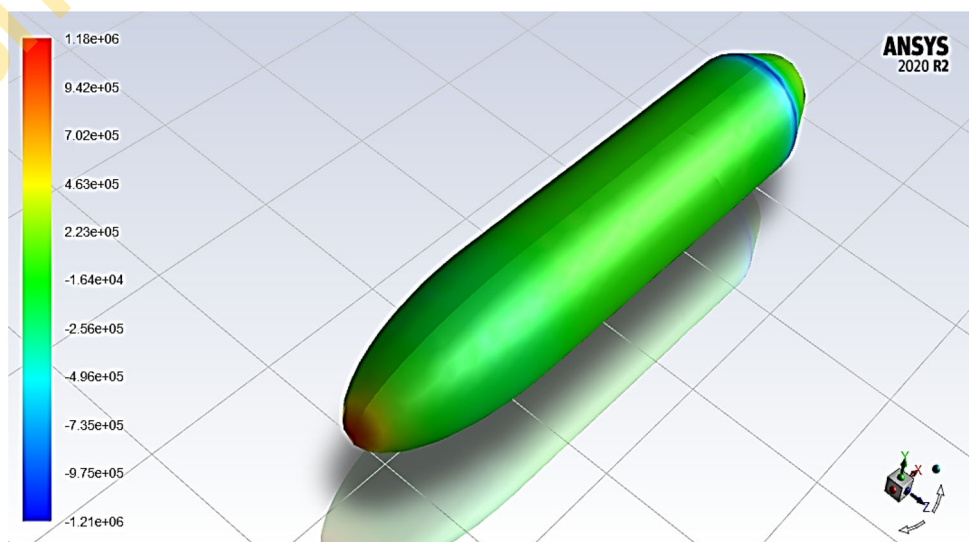


Fig. 22 Pressure contour of conical nose model

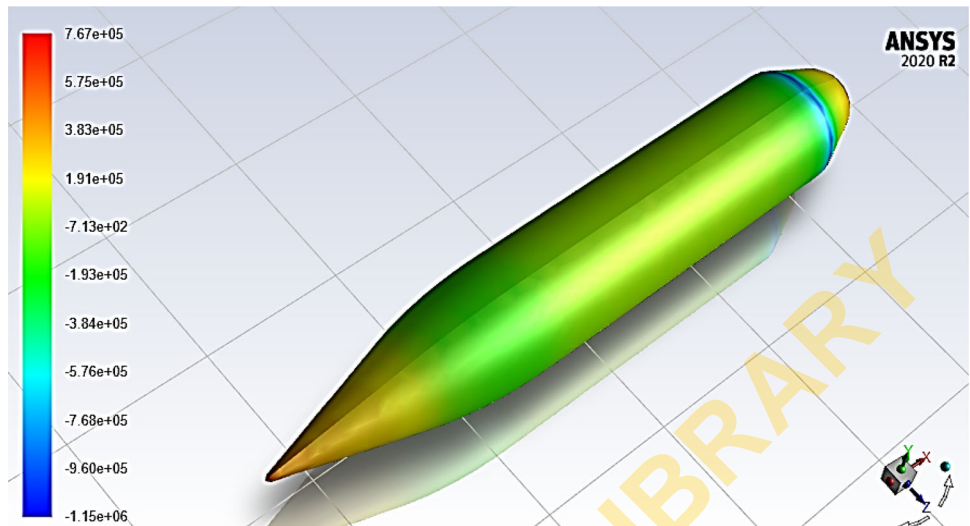


Fig. 23 Drag coefficient comparison of nose models

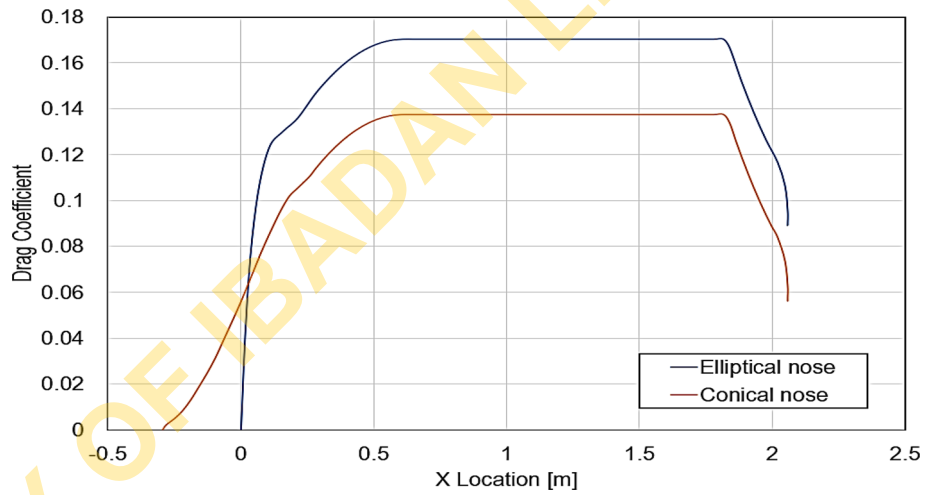


Fig. 24 Pressure contour of NACA 0012 airfoil

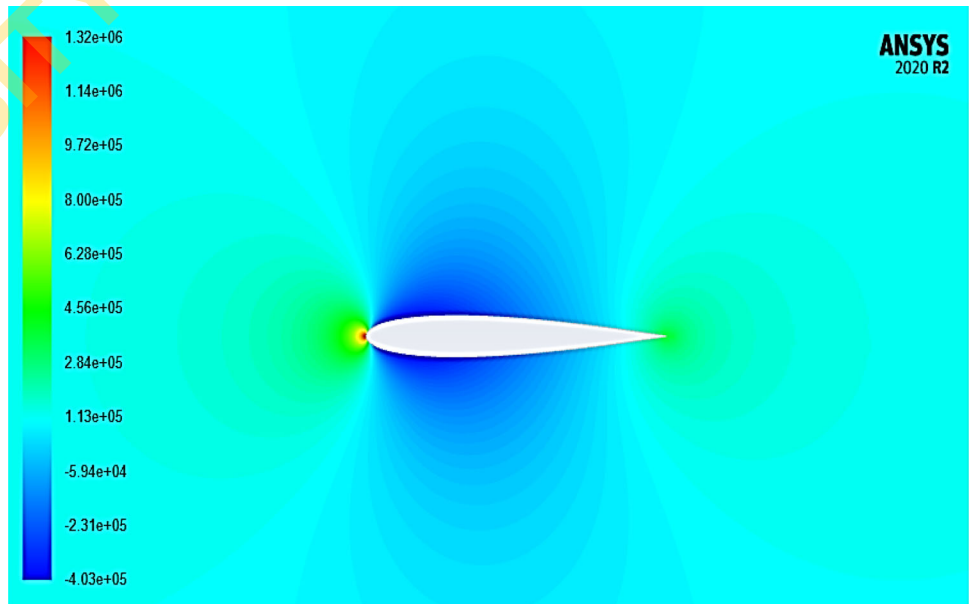


Fig. 25 Pressure contour of wedged NACA 0012 airfoil

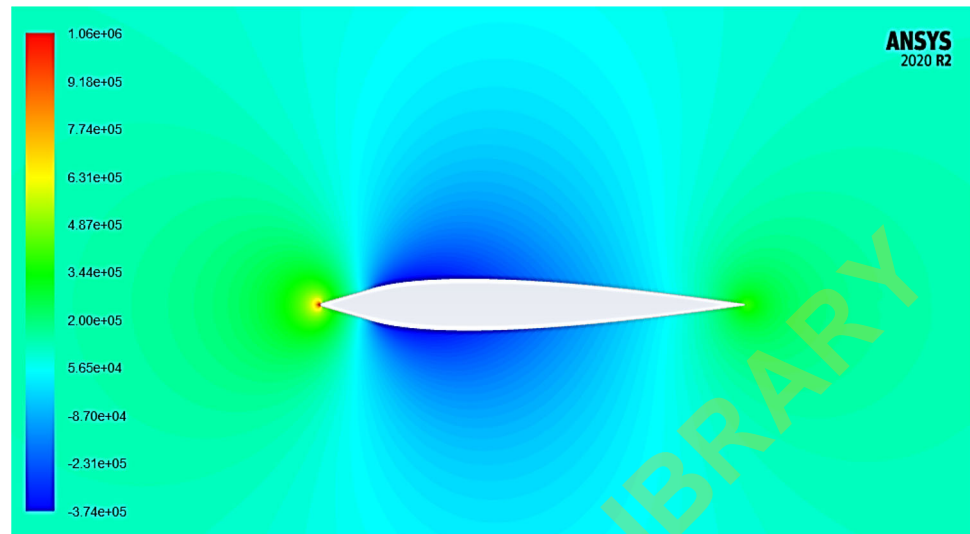
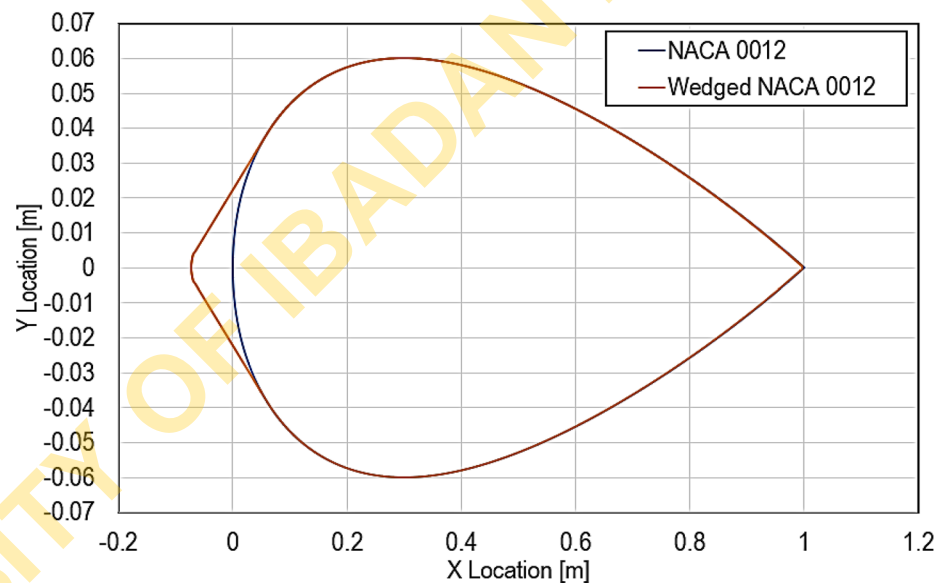


Fig. 26 Geometry plot for the standard NACA 0012 airfoil and similar airfoil with a wedged shape leading edge

NACA airfoil and the wedged airfoil were calculated to be $1.23e-01$ and $8.33e-02$, respectively.



shows evidence of the flow's gradual acceleration, which results in less initial pressure drag in the water than the typical NACA 0012 airfoil. A more abrupt stall point and a lower peak lift coefficient are two aerodynamic challenges brought on by the use of the wedged design. The maximum drag coefficients for the NACA airfoil and the wedged airfoil were calculated to be $1.23e-01$ and $8.33e-02$, respectively.

4.3 Comparing transition approach and submerged flow approach

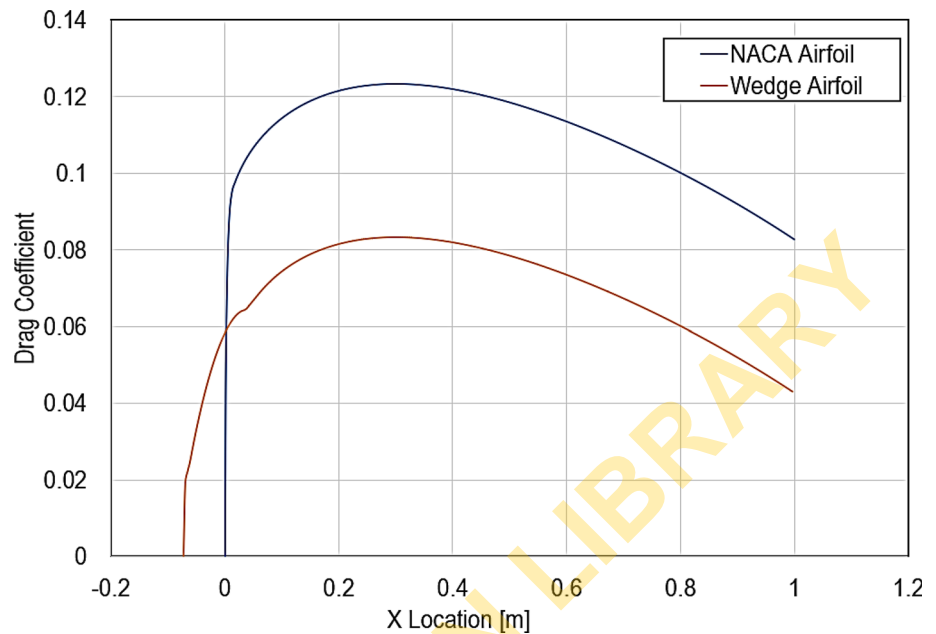
It can be seen that the drag coefficient determined using the submerged case approach significantly underestimates the initial drag when compared to the axisymmetric centre body and the UAV slender centre body. This is because the

approach fails to take into account the sudden acceleration of the water upon entry of the rigid body.

5 Conclusions

To investigate the transition of streamlined bodies, such as 2-D wing shapes and an axisymmetric centre body, from air to water at high velocities, a CFD model was created. Negative volumes that could arise from the dynamic mesh during the transition process was taken care of by using a body-centered mesh. When the computed drag coefficient and experimental data were compared, it was determined that the model was accurate because there was a respectable level of agreement. In order to calculate the impact force on a body during the transition, this study considered both the transition method

Fig. 27 Drag coefficient comparison of airfoils



and the submerged flow method. The transition method based on transient-time analysis was found to be reliable and to have provided vital details regarding the force of impact and cavitation growth. The steady-state analysis of the submerged flow approach allowed for quick understanding of pressure and velocity distribution, but because it did not consider the fluid's initial acceleration, the initial force of impact was underestimated.

According to the results of the CFD simulations performed for the three-dimensional centre bodies using the submerged flow method to examine the impact of nose shape on drag reduction. As a result, it was determined that a sharper nose design reduced drag more successfully. Calculations using the transition approach indicated that the slender body could handle the impact and drag forces, and that this could be done with a sharper and less steep nose section. The study also looked at how the leading-edge design affected the drag and impact forces on the wing bodies as they entered the water. The findings demonstrated that, in comparison to rounded leading edges, which are known to offer better lift characteristics over a range of air angles, wedge-shaped leading edges provided lower impact and drag forces. The wedged and elliptical leading-edge models were used as two representative models to simulate wing bodies. A quarter of the drag of the elliptical leading-edge model was demonstrated by the wedged leading-edge model. It is important to keep in mind that while the mesh used in all simulations could be made finer, doing so would require more computational time and resources.

For further studies, it is recommended to conduct a mesh independence study. The present study focuses on the entry of the object perpendicular to the water surface, which is an

appropriate initial condition for this type of analysis. However, it is important to consider that the power of water current may cause variations in the inclination of the body during water entry, thus it is suggested to investigate different angles of inclination. To gain a better understanding of the performance of a full-body UAV in various conditions, a numerical study of the full body may be conducted. This is particularly important because cavitation would occur at two areas on the body: the wings, and the nose. According to prior research [21], pre-existing disturbances ahead of a rigid body's entry into water can lead to a reduction in impact force. Therefore, it may be worthwhile to simulate a modified leading-edge design that could not only help decrease the impact force but also create a disturbance in the water.

Acknowledgements We appreciate the Research Institute for Autonomous System (RIAS) at University of North Dakota and Northrup Grumman and for their funding support. Any opinions, findings and conclusions or recommendations expressed in this material are those of the author(s) and do not necessarily reflect the views of the funding agencies.

References

1. Retrieve from <https://www.dartdrones.com/blog/difference-between-uav-and-uas/>
2. Retrieved from <https://www.globenewswire.com/en/newsrelease/2021/09/07/2292615/0/en/Unmanned-Aerial-Vehicle-UAV-Market-Size-to-Hit-US-36-Bn-by-2030.html>
3. Retrieved from <https://www.marketsandmarkets.com/Market-Reports/unmanned-aerial-vehicles-uav-market-662.html>
4. Retrieved from https://www.faa.gov/uas/resources/by_the_numbers/
5. Worthington, A.M., Cole, R.S.: V. Impact with a liquid surface, studied by the aid of instantaneous photography. *Philos. Trans.*

- R. Soc. Lond. Ser. A Contain. Pap. Math. Phys. Character **189**, 137–148 (1897)
6. Worthington, A.M.: A Study of Splashes. Longmans, Green, and Company (1908)
 7. Von Karman, T.: The Impact on Seaplane Floats During Landing (1929)
 8. Wagner, V.H.: Impact and sliding processes of fluid on surfaces. *J. Appl. Math. Mechanics* **12**(4), 193–215 (1932)
 9. Mackie, A.G.: A linearized theory of the water entry problem. *Quart. J. Mech. Appl. Math.* **15**(2), 137–151 (1962)
 10. Zhao, R., Faltinsen, O., Aarsnes, J.: Water entry of arbitrary two-dimensional sections with and without flow separation. In: Proceedings of the 21st Symposium on Naval Hydrodynamics, pp. 408–423 (1996)
 11. Tveitnes, T., Fairlie-Clarke, A.C., Varyani, K.: An experimental investigation into the constant velocity water entry of wedge-shaped sections. *Ocean Eng.* **35**(14–15), 1463–1478 (2008)
 12. Nisewanger, C.R.: Experimental determination of pressure distribution on a sphere during water entry. Naval Ordnance Test Station China Lake CA (1961)
 13. Baldwin, J.L., Steves, H.K.: Vertical water entry of spheres. NASA STI/Recon Tech. Rep. N **76**, 13452 (1975)
 14. May, A.: Vertical entry of missiles into water. *J. Appl. Phys.* **23**(12), 1362–1372 (1952)
 15. Shepard, T., Abraham, J., Schwalbach, D., Kane, S., Siglin, D., Harrington, T.: Velocity and density effect on impact force during water entry of sphere. *J. Geophys. Remote Sens* **3**(129), 2169–2249 (2014)
 16. May, A., Woodhull, J.C.: Drag coefficients of steel spheres entering water vertically. *J. Appl. Phys.* **19**(12), 1109–1121 (1948)
 17. Wang, J., Faltinsen, O.M., Lugni, C.: Unsteady hydrodynamic forces of solid objects vertically entering the water surface. *Phys. Fluids* **31**(2), 027101 (2019)
 18. Truscott, T.T., Epps, B.P., Belden, J.: Water entry of projectiles. *Annu. Rev. Fluid Mech* **46**(1), 355–378 (2014)
 19. Lee, M., Longoria, R.G., Wilson, D.E.: Cavity dynamics in high-speed water entry. *Phys. Fluids* **9**(3), 540–550 (1997)
 20. Plesset, M.S., Shaffer, P.A., Jr.: Cavity drag in two and three dimensions. *J. Appl. Phys.* **19**(10), 934–939 (1948)
 21. Rabbi, R., Speirs, N.B., Kiyama, A., Belden, J., Truscott, T.T.: Impact force reduction by consecutive water entry of spheres. *J. Fluid Mech.* **915**, A55 (2021)
 22. Kleefsman, K.M.T., Fekken, G., Veldman, A.E.P., Iwanowski, B., Buchner, B.: A volume-of-fluid based simulation method for wave impact problems. *J. Comput. Phys.* **206**(1), 363–393 (2005)
 23. Fairlie-Clarke, A.C., Tveitnes, T.: Momentum and gravity effects during the constant velocity water entry of wedge-shaped sections. *Ocean Eng.* **35**(7), 706–716 (2008)
 24. Shen, Z., Wan, D.: Numerical simulation of sphere water entry problem based on VOF and dynamic mesh methods. In: The Twenty-first International Offshore and Polar Engineering Conference. OnePetro (2011)
 25. Zhu, X., Faltinsen, O.M., Hu, C.: Water entry and exit of a horizontal circular cylinder (2007)
 26. Zhang, Y., Zou, Q., Greaves, D., Reeve, D., Hunt-Raby, A., Graham, D., Lv, X.: A level set immersed boundary method for water entry and exit. *Commun. Comput. Phys.* **8**(2), 265–288 (2010)
 27. Aquelet, N., Souli, M., Olovsson, L.: Euler–Lagrange coupling with damping effects: application to slamming problems. *Comput. Methods Appl. Mech. Eng.* **195**(1–3), 110–132 (2006)
 28. Maruzewski, P., Touzé, D.L., Oger, G., Avellan, F.: SPH high-performance computing simulations of rigid solids impacting the free-surface of water. *J. Hydraul. Res.* **48**(sup1), 126–134 (2010)
 29. Yan, G., Pan, G., Shi, Y., Zhang, D., Chao, L.: Experimental and numerical investigation of water entry impact forces on air-launched AUV. In: OCEANS 2017-Anchorage, pp. 1–4. IEEE (2017)
 30. Chukwuemeka, E.C.: Numerical Investigation of Forces and Acceleration for Air-Sea UAV in Transition (Doctoral dissertation, The University of North Dakota) (2021)
 31. Yu, P., Shen, C., Zhen, C., Tang, H., Wang, T.: Parametric study on the free-fall water entry of a sphere by using the rans method. *J. Mar. Sci. Eng.* **7**(5), 122 (2019)
 32. Retrieved from <https://www.airfoiltools.com>

Publisher's Note Springer Nature remains neutral with regard to jurisdictional claims in published maps and institutional affiliations.

Springer Nature or its licensor (e.g. a society or other partner) holds exclusive rights to this article under a publishing agreement with the author(s) or other rightsholder(s); author self-archiving of the accepted manuscript version of this article is solely governed by the terms of such publishing agreement and applicable law.